Near-surface velocity modeling using a combined inversion of surface and refracted P-waves

Florian Duret[1], Frederique Bertin[1], Katia Garceran[1], Raphael Sternfels[1], Thomas Bardainne[1], Nicolas Deladerriere[1], and David Le Meur[1]

Abstract

We propose an innovative workflow based on the complementary use of Rayleigh waves alongside standard P-wave refraction tomography, which better depicts the shallow part of the near-surface P-wave velocity model. Our surface-wave processing sequence led to an S-wave near-surface velocity field that can be used as a constraint for P-wave tomography and can improve P-wave statics determination. Rayleigh waves are processed in three steps. The first step consists of an accurate frequency-dependent traveltime measurement for each selected source-receiver pair in which the phase difference between two adjacent traces is used to derive the phase velocity. Then, a frequency-dependent surface-wave velocity tomography is performed from the picked traveltimes. Finally, after surface-wave tomography, the frequency-dependent phase velocity volume output by the tomography is inverted to deliver an S-wave near-surface velocity model. This model is used to constrain the first-arrival P-wave tomography. To illustrate our method, we use a 3D narrow-azimuth land data set, acquired along a river valley. Strong lateral velocity variations exist in the shallow part, with slow velocities around the unconsolidated sediments of the riverbed and faster velocities in the consolidated sediments of the surrounding hills. A combined first-arrival tomography using the S-wave velocity model, the initial unconstrained refracted P-wave velocity model, and the original first arrivals is used to obtain a more accurate near-surface P-wave velocity model. This new approach led to a constrained P-wave velocity model from which primary statics are derived and then applied, leading to an improved image with better focusing and continuity of thin layers in the shallowest part.

Introduction

The estimation of geologically meaningful near-surface P-wave velocity models can be challenging on land surveys due to rapid lateral variation in near-surface structures. Approaches based on refracted P-waves, such as first-arrival traveltime tomography (Noble et al., 2009; Taillandier et al., 2011), usually lack resolution in the shallow part of the medium because of the horizontal nature of the diving waves, although recent advances in full-waveform inversion (Virieux and Operto, 2009) show promising results in that respect. To overcome this issue, surface-wave inversion has become increasingly popular (Socco and Strobbia, 2004; Socco et al., 2010). Indeed, surface waves are very sensitive to lateral variations, especially in the shallowest parts of the near surface. An analysis may provide access to the S-wave velocity structure at depth, but it is difficult to link it with the P-wave velocity structure.

We propose a new workflow where a combined P-wave tomography better depicts the velocity contrasts in the near surface. Our proposed method's effectiveness is demonstrated on a 3D narrow-azimuth land survey acquired around a wide meandering river (Figure 1). A standard acquisition design was used, with a 20 m interval in the inline direction and 300 m interval in the crossline direction for both source and receiver spreads. This method was used to compute a P-wave velocity model from which primary P-wave statics are derived. We then explain in detail the surface-wave inversion workflow and the combined P-wave tomography. Finally, we show a comparison of two stack sections extracted from the survey around the river path — the first with primary P-wave static corrections computed from the standard, unconstrained P-wave velocity model; the second with corrections computed from our improved, constrained P-wave velocity model.

Refracted P-wave workflow

The refracted P-wave workflow consists of accurately picking first-break arrival times, then performing a nonlinear traveltime tomography (Zhang and Toksöz, 1998) to obtain a standard conventional near-surface P-wave velocity model (Figure 2a). First-arrival traveltimes t^{obs} are picked for each trace (Figure 3a), then the tomography algorithm iteratively updates the near-surface velocity model c by minimizing a misfit function $J(c)$ between the observed traveltimes t^{obs} and modeled traveltimes $t(c)$. Typically, a least-squares misfit function is used:

$$J(c) = \frac{1}{2}(t(c) - t^{obs})^t (t(c) - t^{obs}) \quad . \tag{1}$$

Picking the first-arrival traveltimes is usually performed automatically due to the high number of traces involved and can be contaminated by some erroneous picks caused by high levels of noise in the input data. To reduce the influence of such erroneous picks in the minimization process, we use a more robust L1 misfit function in our applications:

$$J(c) = \left\| t(c) - t^{obs} \right\|_1 = \Sigma \left| t_i(c) - t_i^{obs} \right| \quad . \tag{2}$$

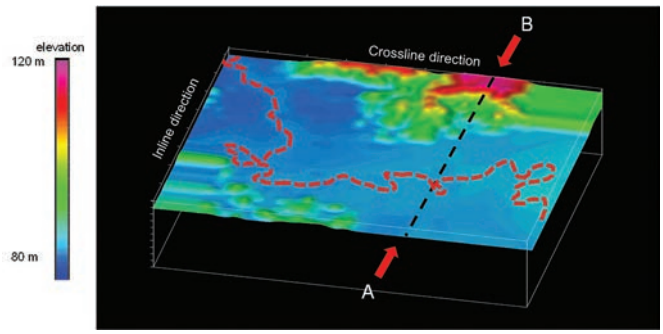

Figure 1. Elevation map around the survey. It is a river valley surrounded by swamp terrain (main river channel denoted by red dashed line) bordered by small hills. The dashed black line A-B denotes the shot line used to illustrate the approach presented in this paper.

[1]CGG.

http://dx.doi.org/10.1190/tle35110946.1.

In this work, we employ an accurate eikonal solver based on the fast sweeping method (Noble et al., 2014) to compute the first-arrival traveltimes $t(c)$ for a given velocity model c. The gradient $\nabla J(c)$ of the misfit function is computed on-the-fly by back-propagating the residuals along rays from the receiver points to the source, hence avoiding the need to build and store a very large Jacobian matrix (Taillandier et al., 2011). The misfit function $J(c)$ is then iteratively minimized using a limited-memory Broyden–Fletcher–Goldfarb–Shanno (L-BFGS) optimization algorithm (Nocedal and Wright, 2006), which uses gradients from previous iterations to build a computationally efficient approximation to the Hessian, allowing for better-quality model updates compared to previously employed steepest-descent schemes.

Although we implemented an eikonal-based P-wave tomography using a gridded velocity model, other modeling engines can be used — e.g., to employ layered or blocky models such as in Vesnaver et al. (2006). In this work, we used a grid spacing of 80 m in the inline and crossline direction and 20 m in the depth direction for the P-wave velocity model, and we added a smoothing regularization to stabilize the inversion. A 70 m depth slice through the obtained P-wave velocity model is shown in Figure 3b. Both main features (riverbed and surrounding hills) are easily identified, but the model lacks resolution to clearly identify lateral velocity variations around the river. Nevertheless, the introduction of primary statics computed from this velocity model significantly improves the lateral coherency of the stack as shown in Figure 4. Figure 4a presents the raw stack along a section that follows the river path; figure 4b illustrates the improvement obtained by application of P-wave statics. The lateral coherency of the events is clearly improved (red arrows), but some parts of the stack section remain blurry (dashed circle). This is because of rapid shallow velocity variations that are not properly resolved by the employed P-wave tomography. Indeed, due to the deep reflection seismic acquisition design (360 m and 280 m interval for both source and receiver lines) and the fact that the 0–100 m offset class represents only 0.01% of the picked times, the refracted P-wave tomography used is not able to properly characterize structures and velocity variations in the shallowest part of the near surface. Weak ray coverages are observed in the first 100 meters (Figure 3c), indicating that the shallowest area of the P-wave velocity model is under-constrained and would restrict the statics resolution.

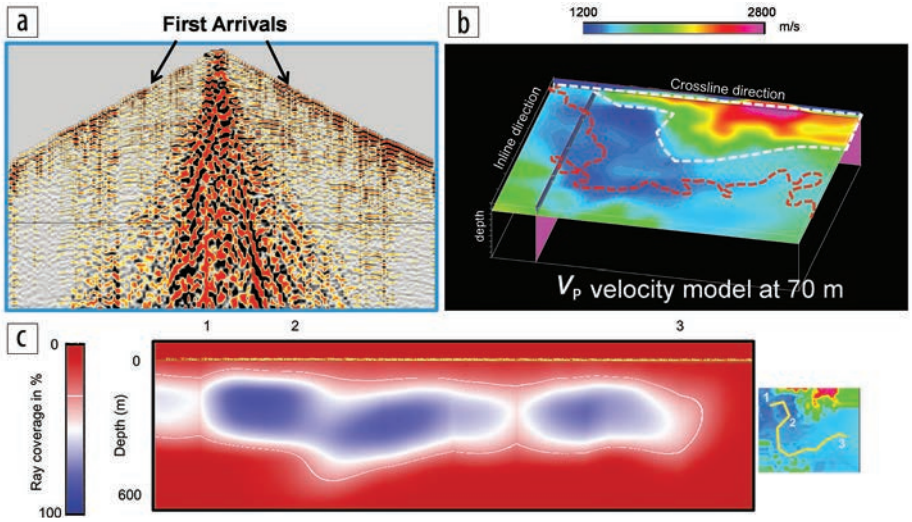

Figure 3. (a) First arrivals observed along the receiver line A-B (see Figure 1). (b) The refracted P-wave velocity model obtained with the standard refracted P-wave modeling workflow. The red dashed line marks the river; surrounding hills are delimited by the white dashed line. (c) Ray coverage depth section along the river path 123 where weak ray coverages (< 30%) are observed on the first 100 meters.

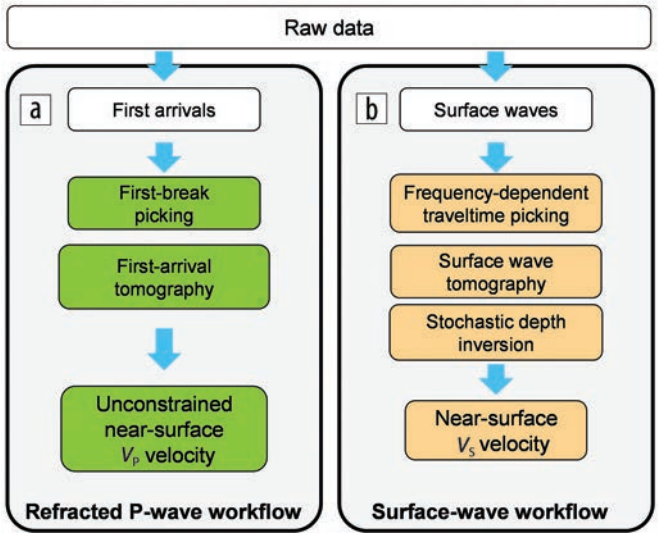

Figure 2. Flowchart of (a) a refracted P-wave modeling workflow and (b) surface-wave modeling workflow.

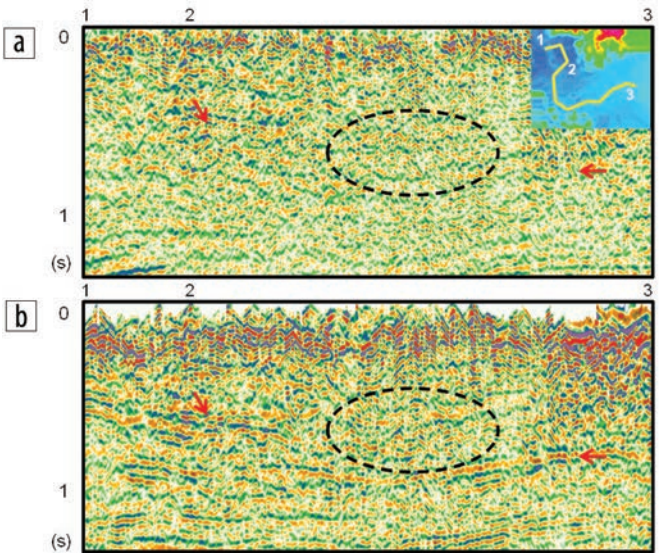

Figure 4. Stack section along the river path line 123 (map in top right corner). (a) Stack obtained without applying any static correction. (b) Stack obtained after application of primary statics derived from the conventional P-wave velocity model. The overall lateral coherency is improved (red arrows), but some parts remain blurry (dashed circle) due to rapid lateral variations in the near-surface structure.

Surface-wave workflow

As shown earlier, there are complex lateral velocity variations in the shallow near surface. The computation of a reliable shear-wave velocity (V_S) model therefore could bring valuable additional information to validate and better constrain the refracted P-wave velocity (V_P) model. Our surface-wave workflow consists of frequency-dependent traveltime picking, followed by frequency-dependent traveltime tomography, and, finally, a stochastic depth inversion (Figure 2b).

First, conventional preprocessing is applied to separate surface waves from the recorded data (Le Meur et al., 2008) using the raw input data (Figure 5). This preprocessing is aimed at partially attenuating any spatial aliasing and enhancing the linearity and signal-to-noise ratio of the Rayleigh waves. Only short offsets (less than 1 km) are used for the frequency-dependent traveltime picking of the Rayleigh waves in order to ensure a robust picking of the most energetic surface-wave mode.

Accurate frequency-dependent traveltimes are computed for each selected source-receiver pair (first orange box in Figure 2). To do so, the principle of a multi-offset phase analysis (MOPA) described by Strobbia and Foti (2006) is used. The MOPA approach is a generalization of the well-known spectral analysis of surface waves (SASW) (Nazarian and Stokoe, 1984) in which the phase difference between two adjacent traces is used to derive the phase velocity (Socco et al., 2010). This offers an interesting alternative to a multistation approach, for example, the slant-stack or *fk* methods introduced in the 1980s (McMechan and Yedlin, 1981; Gabriels et al., 1987). Although these multistation approaches are able to identify all propagation modes, there remains the difficulty of picking the different modes with confidence, especially for noisy land data in which rapid lateral velocity variations are observed. Such approaches have been used successfully for shallow marine or ocean-bottom-node data (Zheng and Miao, 2014) but not necessarily for land data. On the contrary, on onshore data, MOPA is able to accurately pick the most energetic propagation mode, which most often corresponds to the fundamental one. To demonstrate the effectiveness of this approach for computing frequency-dependent traveltimes, we need to ensure that the dispersion curve on the most energetic mode is robust and accurate enough compared to conventional approaches.

The main assumption in the MOPA approach is that the modal phase for one single mode of propagation can be decomposed as:

$$\varphi_i(\omega, x) = -k(\omega).x_i + \varphi_0(\omega), \tag{3}$$

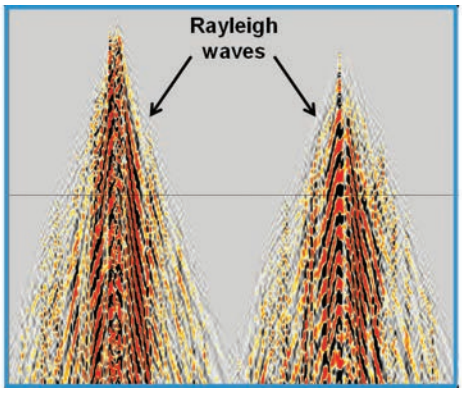

Figure 5. Rayleigh waves observed along the AB shot line (see Figure 1) after extraction from the raw data shown in Figure 3a.

where $\varphi_i(\omega,x)$ is the phase of the single mode of propagation, $k(\omega)$ is the associated wavenumber, $\varphi_0(\omega)$ is the phase of the source, x_i is the offset i, and ω is the angular frequency.

From equation 3, it appears that the phase-versus-offset data at a single frequency $f = \omega/2\pi$ can be used to estimate the wavenumber using a linear regression. Then, from the estimated $k(\omega)$ values, it becomes possible to compute the phase velocity as a function of frequency:

$$V(\omega) = \frac{\omega}{k(\omega)} = \frac{2\pi f}{k(\omega)}. \tag{4}$$

If we now combine N receivers and unwrap the phase, at each frequency, in the increasing offset direction, we obtain a system of equations that can be inverted in the least-squares sense (Strobbia and Foti, 2006). A robust estimation of the wavenumber and phase velocity is thus obtained. To control the quality of the fit to the linear model at every frequency, we used the coefficient of determination R^2 (equation 5). This coefficient varies between 0 and 1, where a value of 1 indicates a perfect fit to the linear model, and a zero value indicates the absence of linearity. To improve the estimation of phase velocities for real land data sets, variable offset ranges and azimuthal sectors are introduced to maximize the fit to a linear model. Then, the whole problem turns into a maximization process: for each azimuthal sector, the goal is to find the minimum offset i and maximum offset j that maximize:

$$R^2(i,j) = \frac{\Sigma_{k=i}^{j}\left(\widehat{\varphi k} - \bar{\varphi}\right)^2}{\Sigma_{k=i}^{j}\left(\varphi k - \bar{\varphi}\right)^2}, \tag{5}$$

where $R^2(i,j)$ is the coefficient computed at offset i and j. $\widehat{\varphi_k}$ is the predicted value of the phase at offset k, $\bar{\varphi}$ is the average of the observed values, and φ_k is the observed value of the phase at offset k.

Then, the best phase/offset pairs are retained for determination of the phase velocity for selected frequencies, reducing the influence of phase unwrapping errors on the linear regression operation. A validation of this approach is performed using 2D synthetic data where we clearly identify the Rayleigh-wave fundamental mode and first higher modes (Figure 6a). To compare the dispersion curve obtained with the MOPA approach, the dispersion panels of all Rayleigh-wave modes are computed using a multistation slant-stack method (Figure 6b). In this synthetic data test, a perfect match is observed between the maxima of both dispersion curves corresponding to the fundamental mode (red superimposed curve for MOPA, Figure 6).

Finally, for every frequency, traveltime picks are derived from the computed phase velocities using the average distance between each selected source (i) and receiver (j):

$$t_{ij}(\omega) = \frac{\widehat{\dot{x}_{ij}}}{V(\omega)}. \tag{6}$$

Our picking strategy for a 3D narrow-azimuth survey involves all available source-receiver pairs (SR_i) for each shot (S) and several

azimuths (az). For every frequency (ω), traveltime picks $T_{Raz}(SR_i,\omega)$ are retained at each source-receiver midpoint value (Figure 7). All traveltime picks from all frequencies, sources, and receivers are then used to feed the surface-wave tomography.

For refracted P-wave velocities, the individual measurements made on discrete source-receiver pairs need to be generalized on the model grid. To handle the particularities of Rayleigh waves, the algorithm used is a modified version of refracted P-wave tomography. Although surface waves are the consequence of complex 3D wave interactions, the direct and inverse problem can be approximated in 2D. To take into account the surface-wave dispersion evident in frequency-dependent picking, the tomography is performed frequency by frequency (second orange box in Figure 2b). For each frequency, we used a grid with a spacing of 80 m in each inline and crossline direction to describe the Rayleigh-wave velocity model. Each 2D-based tomography inversion (associated with a given angular frequency ω) reveals the averaged Rayleigh velocity between the free surface and its penetration depth. The obtained 3D volume $V_S(x,y,\omega)$ is then introduced in the vertical depth inversion procedure. The benefit of such tomography is illustrated on a frequency slice at 4.5 Hz (Figure 8a), which corresponds to the shallow part of the near surface. After the Rayleigh-wave traveltime tomography, the river channel is well identified (dashed red line), with fairly slow-phase velocity on the surface-wave tomography (~200 m/s) and higher-phase velocity (~600 m/s) corresponding to the root of the surrounding hills (white dashed line). Strong depth coverages are observed in the first 200 meters (Figure 8c), indicating that the shallowest area of the S-wave velocity model is well-constrained.

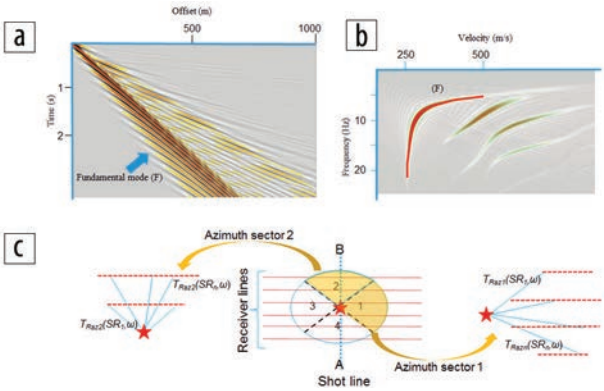

Figure 6. (a) A synthetic shot with Rayleigh-wave fundamental mode (F) and higher modes. (b) Dispersion panel computed from a multistation slant-stack approach; all dispersion curves from the Rayleigh waves are clearly identified. The dispersion curve computed by MOPA is superimposed in red on the dispersion panel. (c) Picking strategy used for a 3D shot. After splitting into four azimuths, MOPA was performed using the selected source and receiver pairs and their associated offset values. On azimuths 1 and 2, a zoomed section shows how each source and receiver pair from different azimuths are computed.

The last tool used in the surface-wave inversion workflow is a stochastic depth inversion (third orange box in Figure 2). During this step, a depth-dependent S-wave velocity cube $V_S(x,y,z)$ is computed from the frequency-dependent surface-wave velocity volume $V_R(x,y,\omega)$. For each node (x,y) of the tomography grid, the surface-wave dispersion curve $V_R(\omega)$ is inverted to obtain a vertical depth S-wave velocity profile $V_S(z)$. Few nonlinear approaches have been described to obtain a depth S-wave velocity profile (Hou et al., 2016; Maraschini and Foti, 2010). We decided to implement a Markov-chain Monte Carlo algorithm (Shapiro et al., 1997), associated with a forward modeling method based on the formulation of the relation between a vertical S-wave velocity profile and associated surface-wave dispersion curves as proposed by Schwab and Knopoff (1972). The initial model is a layered S-wave velocity profile, composed of three constant-velocity layers (Figure 9a, red curve) on top of an infinite half-space. A random perturbation is applied to either the depth or the velocity of the layer to obtain a candidate model, and the associated surface-wave dispersion curve is deduced. This candidate dispersion curve is then compared to the observed dispersion curve $V_R(\omega)$. If the distance between them is small enough, the candidate dispersion curve is accepted, and the corresponding model is used to generate the next random model; if not, it is rejected, and we reuse the previous accepted model and continue perturbing it until an acceptable new model is found. This operation is iterated until a sufficient number

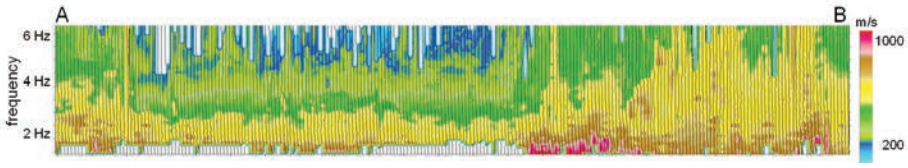

Figure 7. Fundamental-mode Rayleigh-wave picks located at the midpoint location for all source-receiver pairs along the shot line A-B. High frequencies (which sample shallow structures) are plotted at the top, while lower frequencies (which sample deeper layers) are plotted at the bottom. A high lateral variability is observed at higher frequencies, while variations are smoother for lower frequencies.

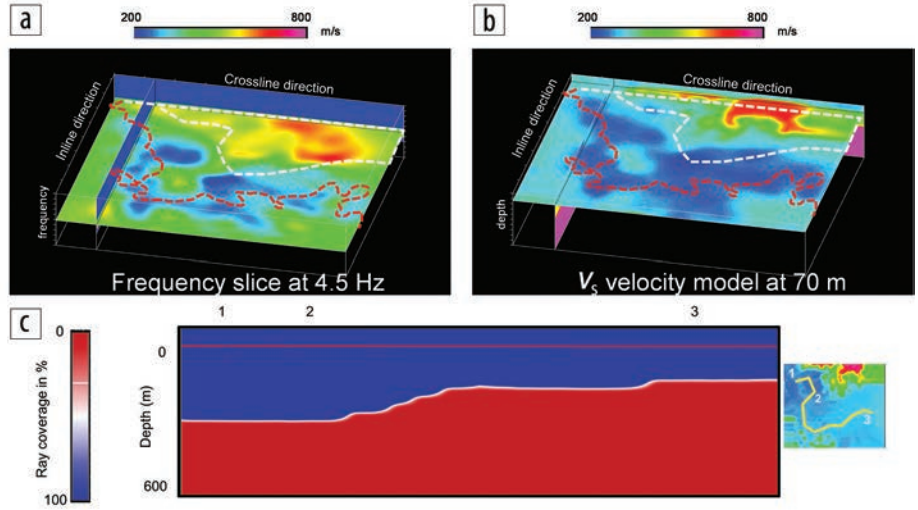

Figure 8. (a) Frequency slice at 4.5 Hz after eikonal-based 2D traveltime tomography. (b) Depth S-wave velocity model at 70 m obtained after Markov-chain Monte Carlo inversion. (c) Depth coverage section along the river path 123 where the maximum ray coverage is observed on the first 200 meters.

(typically a few thousand) of suitable S-wave velocity profiles are obtained at each node (*x*,*y*) of the tomography grid (Figure 9, gray curves). The final S-wave velocity cube $V_S(x,y,z)$ is the set of vertical S-wave velocity profiles that best explain the dispersion curves observed at their respective nodes (*x*,*y*) (Figure 9a, blue curve). The final depth S-wave velocity model is obtained after a stochastic inversion as illustrated in Figure 8b. The river channel location is also clearly identified on the depth slice at 70 m where slow S-wave velocities (~250 m/s) are surrounded by faster S-wave velocities (~350 m/s), which correspond to the hills shown on the elevation map (Figure 1).

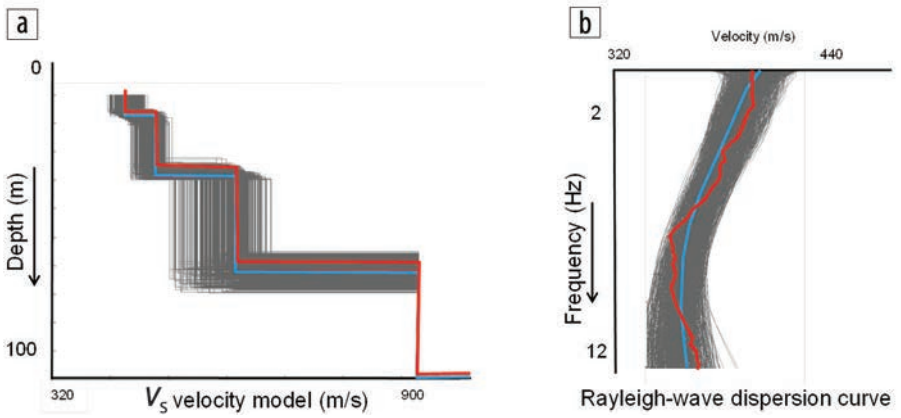

Figure 9. (a) V_S velocity model; in red the initial model, in gray all generated models, in blue the best-fit model. (b) Rayleigh-wave dispersive curve; in red the measured dispersion curve, in gray the computed curves associated with the generated models, in blue the curve associated with the best-fit model.

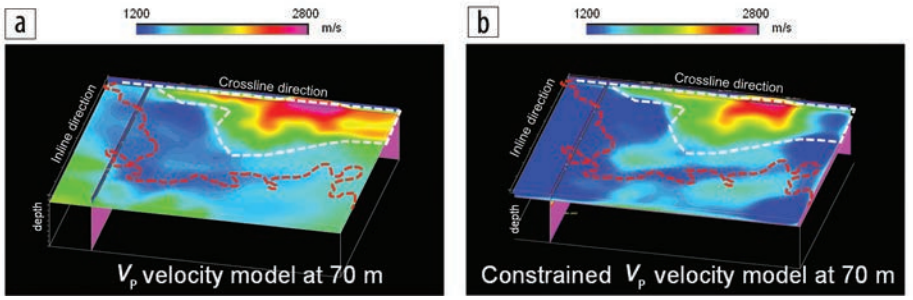

Figure 10. (a) Refracted P-wave velocity model at 70 m obtained after a standard first-arrival traveltime tomography. (b) The constrained refracted P-wave velocity model at 70 m obtained after the combined inversion.

Combined refracted P-wave tomography

We observe that the depth S-wave velocity model (Figure 8b) provides more accurate spatial resolution in the shallowest part. On the 70 m depth slice, the river channel's path is clearly identified on the depth S-wave velocity model but is more difficult to define on the standard refracted P-wave velocity model (Figure 3b). At this point, it is interesting to compare the resolution obtained from both workflows in the shallowest part of the near-surface. The difference observed on the final results is explained by the ray and depth coverage of both tomography methods (Figure 3c and Figure 8c). Indeed, the resolution of the refracted P-wave tomography is weaker in the first 100 m due to the seismic acquisition design (figure 3c). Conversely, this design is sufficient for surface-wave processing. Considering that the penetration depth of Rayleigh waves is linked to the frequency range (from 2 to 10 Hz in this case) and its associated phase velocities (from 600 to 200 m/s in this case), we can expect to obtain a better resolution than refracted P-waves in the first 200 m (Figure 8c).

Taking these observations into account, our strategy of combining P-waves and Rayleigh waves is simple: instead of using a smooth and underdetermined V_P for the first 100 meters of the velocity model, we prefer to use V_S information from the surface wave inversion with a regional V_P/V_S ratio estimated from the overlap zone between the V_P and V_S velocity model (here a ratio of 3 is used). Although this ratio remains inaccurate, it helps provide additional structural information on the shallowest part. Ideally, uphole measurements and/or any other local V_P/V_S ratio information would be very useful and relatively easy to introduce in such a combined method. Unfortunately, such data were not available on this survey. In this case study, the additional details brought by an S-wave velocity model enhance the spatial resolution of the final refracted P-wave model by better constraining the tomography inversion. The deepest part of the velocity model is kept unchanged below the maximum depth penetration observed on the depth S-wave velocity model (figure 10), which is linked to the lowest observed frequency and associated velocity of the surface waves. To do so, the original refracted P-wave first arrivals are used to compute the final constrained refracted P-wave velocity model. The results obtained in the shallowest part (here at the same 70 m depth slice) after the combined workflow are highlighted in Figure 10b. Indeed, small velocity variations from the S-wave velocity model are retained on the constrained refracted P-wave velocity model (Figure 10b). Now, a finer spatial resolution around the river channel and a change in the background velocity are obtained, while higher velocity is maintained under the hills (delimited by the white dashed line).

The higher lateral resolution observed after the combined inversion needs to be validated on seismic data through the application of primary static corrections. It allows us to visualize the impact of a new set of primary static corrections from the combined workflow. Our main zone of interest is the shallow part of the stack section (up to 1.5 s), where the vertical raypath assumption is still valid. Primary static corrections computed from the standard but unconstrained refracted P-wave velocity model show a major improvement in the focusing of events compared to the raw stack (Figure 4a). Application of the new set of primary statics derived from the constrained refracted P-wave velocity model implies an even better lateral continuity of the thin layers (Figure 11, black circle) and also solves cycle skipping of main events (Figure 11, red arrows). This 3D example demonstrates the benefit of the combined first-arrival tomography using information from the depth S-wave velocity model to better characterize the shallow part of the refracted P-wave velocity model.

Conclusions

To improve on standard P-wave refraction tomography, we propose a combined workflow based on the complementary use of Rayleigh waves and refracted P-waves to better characterize the near-surface. Geologically meaningful S-wave and refracted P-wave velocity volumes could be obtained even on narrow-azimuth land data. An accurate frequency-dependent traveltime picking followed by a frequency-dependent surface-wave velocity tomography has brought improvements to the subsequent stochastic inversion in terms of stability and lateral consistency. More reliable depth S-wave and refracted P-wave velocity models bring valuable information to obtain a constrained refracted P-wave velocity model via a combined first-arrival tomography. These benefits apply to 3D land data, even when not well-sampled spatially. This workflow contributes to a better understanding of the near surface, leading to an accurate P-wave velocity model for use in subsequent processing steps such as elastic full-waveform inversion or depth imaging. TLE

Acknowledgments

We are grateful to Ecopetrol of Columbia for permission to present the data examples. We also thank CGG for permission to publish our results. Special thanks to Thomas Hertweck, Pierre Hugonnet, Xiao-Gui Miao, Sara Pink-Zerling, Luke Twigger, and Richard Wombell for their constructive help and suggestions during preparation of this paper.

Corresponding author: david.lemeur@cgg.com

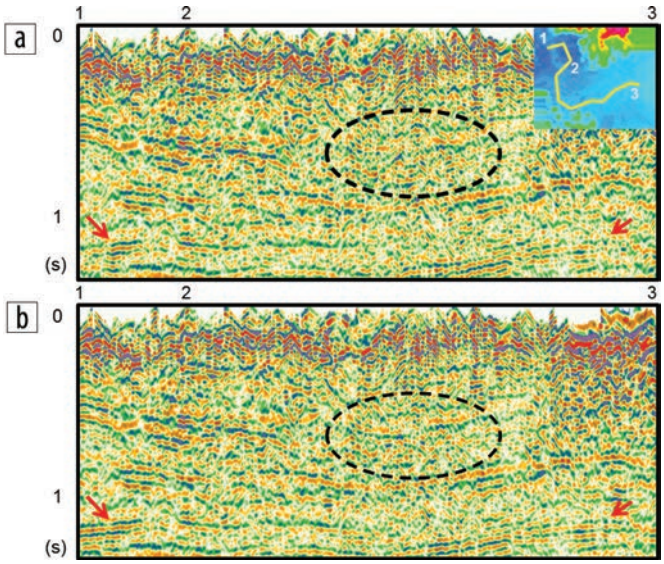

Figure 11. Stack along the river path 123 with (a) the application of primary statics derived from the standard but unconstrained refracted P-wave velocity model and (b) with the application of a new set of primary statics from the constrained refracted P-wave velocity model, where a better lateral continuity in the thin layers is observed (black circle) and also cycle-skipping is solved (red arrows).

References

Gabriels, P., R. Snieder, and G. Nolet, 1987, In situ measurements of shearwave velocity in sediments with higher-mode Rayleigh waves: Geophysical Prospecting, **35**, no. 2, 187–196, http://dx.doi.org/10.1111/j.1365-2478.1987.tb00812.x.

Hou, S., D. Zheng, X. G. Miao, and R. Haacke, 2016, Multimodal surface wave inversion and application to North Sea OBN data: 78th Conference and Exhibition, EAGE, Extended Abstracts.

Le Meur, D., N. Benjamin, R. Cole, and M. Harthy, 2008, Adaptive groundroll filtering: 70th Conference and Exhibition, EAGE, Extended Abstracts, http://dx.doi.org/10.3997/2214-4609.20147745.

Maraschini, M., and S. Foti, 2010, A Monte Carlo multimodal inversion of surface waves: Geophysical Journal International, **182**, no. 3, 1557–1566, http://dx.doi.org/10.1111/j.1365-246X.2010.04703.x.

McMechan, G. A., and M. J. Yedlin, 1981, Analysis of dispersive wave by wave field transformation: Geophysics, **46**, no. 6, 869–874, http://dx.doi.org/10.1190/1.1441225.

Nazarian, S., and K. H. Stokoe II, 1984, In situ shear wave velocities from spectral analysis of surface waves: 8th Conference on Earthquake Engineering, **3**, 31–38.

Noble, M., N. Belayouni, and H. Chauris, 2009, First arrival traveltime tomography for complex near-surface velocity structures: 71st Conference and Exhibition, EAGE, Extended Abstracts, http://dx.doi.org/10.3997/2214-4609.201404930.

Noble, M., A. Gesret, and N. Belayouni, 2014, Accurate 3-D finite difference computation of traveltimes in strongly heterogeneous media: Geophysical Journal International, **199**, no. 3, 1572–1585, http://dx.doi.org/10.1093/gji/ggu358.

Nocedal, J., and S. J. Wright, 2006, Numerical Optimization, 2nd ed.: Springer.

Schwab, F. A., and L. Knopoff, 1972, Fast surface wave and free mode computations, in B.A. Bolt, B. Alder, and S. Fernbach, eds., Methods in Computational Physics, **11**, Academic Press, 87–180.

Shapiro, N. M., M. Campillo, A. Paul, S. K. Singh, D. Jongmans, and F. J. Sanchez-Sesma, 1997, Surface-wave propagation across the Mexican Volcanic Belt and the origin of the long-period seismic-wave amplification in the Valley of Mexico: Geophysical Journal International, **128**, no. 1, 151–166, http://dx.doi.org/10.1111/j.1365-246X.1997.tb04076.x.

Socco, L. V., and C. Strobbia, 2004, Surface-wave method for near-surface characterization: a tutorial: Near Surface Geophysics, **2**, no. 22, 165–185, http://dx.doi.org/10.3997/1873-0604.2004015.

Socco, L. V., S. Foti, and D. Boiero, 2010, Surface wave analysis for building near-surface velocity models – Established approaches and new perspectives: Geophysics, **75**, no. 5, 75A83–75A102, http://dx.doi.org/10.1190/1.3479491.

Strobbia, C., and S. Foti, 2006, Multi-offset phase analysis of surface waves data (MOPA): Journal of Applied Geophysics, **59**, no. 4, 300–313, http://dx.doi.org/10.1016/j.jappgeo.2005.10.009.

Taillandier, C., N. Deladerrière, A. Therond, and D. Le Meur, 2011, First arrival traveltime tomography – When simpler is better: 73rd Conference and Exhibition, EAGE, Extended Abstracts, http://dx.doi.org/10.3997/2214-4609.20149305.

Vesnaver, A., R. Bridle, B. Henry, R. Ley, R. Rowe, and A. Wyllie, 2006, Geostatistical integration of near-surface geophysical data: Geophysical Prospecting, **54**, no. 6, 763–777, http://dx.doi.org/10.1111/j.1365-2478.2006.00573.x.

Virieux, J., and S. Operto, 2009, An overview of full-waveform inversion in exploration geophysics: Geophysics, **74**, no. 6, WCC1–WCC26, http://dx.doi.org/10.1190/1.3238367.

Zhang, J., and M. N. Toksöz, 1998, Nonlinear refraction traveltime tomography: Geophysics, **63**, no. 5, 1726–1737, http://dx.doi.org/10.1190/1.1444468.

Zheng, D., and X. G. Miao, 2014, Multimodal Rayleigh wave dispersion curve picking and inversion to build near surface shear wave velocity models: 76th Conference and Exhibition, EAGE, Extended Abstracts, http://dx.doi.org/10.3997/2214-4609.20140538.